Hindawi
Advances in Civil Engineering
Volume 2019, Article ID 5476909, 17 pages
https://doi.org/10.1155/2019/5476909

Research Article

Seismic Performance of Full-Scale Joints Composed by Concrete-Filled Steel Tube Column and Reinforced Concrete Beam with Steel Plate-Stud Connections

Zhenbao Li,[1] **Yashuang Liu**,[1] **Hua Ma**,[1] **Qianqian Wang**,[2] **and Zhenyun Tang**[1]

[1]*The Key Laboratory of Urban Security and Disaster Engineering, Ministry of Education, Beijing University of Technology, Beijing 100124, China*
[2]*College of Exploration Technology and Engineering, Hebei GEO University, Shijiazhuang 050031, China*

Correspondence should be addressed to Hua Ma; mahua@bjut.edu.cn

Received 20 December 2018; Revised 19 February 2019; Accepted 27 February 2019; Published 18 March 2019

Academic Editor: Raffaele Landolfo

A concrete-filled steel tube (CFST) column has the advantages of high bearing capacity, high stiffness, and good ductility, while reinforced concrete (RC) structure systems are familiar to engineers. The combinational usage of CFST and RC components is playing an important role in contemporary projects. However, existing CFST column-RC beam joints are either too complex or have insufficient stiffness at the interface, so their practical engineering application has been limited. In this study, the results of a practical engineering project were used to develop two kinds of CFST column-RC beam joints that are connected by vertical or U-shaped steel plates and studs. The seismic performance of full-scale column-beam joints with a shear span ratio of 4 was examined when they were subjected to a low-cyclic reversed loading test. The results showed a plump load-displacement curve for the CFST column-RC beam joint connected by steel plates and studs, and the connection performance satisfied the building code. The beam showed a bending failure mode similar to that of traditional RC joints. The failure area was mainly concentrated outside the steel plate, and the plastic hinge moved outward from the ends of the beam. When the calculated cross section was set at the ends of the beam, the bending capacity of joints with the vertical or U-shaped steel plates and studs increased compared to the RC joint. However, when the calculated cross section was set to the failure area, the capacity was similar to that of the RC joint. The proposed joints showed increases in the energy dissipation, average energy dissipation coefficient, and ductility coefficient compared to the RC joint.

1. Introduction

Concrete-filled steel tube (CFST) columns are widely used in practical engineering because of their excellent constructability, such as reduced labor and materials, lack of formwork, and quick construction. In addition, CFST columns provide a high bearing capacity, good ductility, and toughness [1–3]. Considering the common use of beams and slabs, CFST columns with RC beams and RC slabs are an optimal choice for buildings. However, there have been relatively few engineering applications of CFST columns joined to reinforced concrete (RC) beams because of the complex construction of the joint and difficulty with forming a rigid connection.

In contrast to the comprehensive research on CFST column-steel beam joints [4–8], CFST column-RC beam joints have received little attention in the published literature. According to the moment transfer between beams and columns, joints can be divided into three categories: rigid, semirigid, and pinned [9, 10]. Xiang and Lv [11] summarized the existing forms of CFST column-RC beam joints and classified them into these three categories. Based on the results of experimental research and engineering applications, Cai and Huang [12] analyzed the working mechanism and mechanical properties of existing CFST column-RC beam joints. Lu et al. [13] discussed types of joints for the frame structure system and proposed corresponding calculation methods and suggestions for reference in

engineering design and applications. Fang et al. [14] proposed adding a ring beam outside the CFST column with longitudinal reinforcements of the slab beam anchored to the ring beam: the ring beam resists the bending moment of the RC beam by bearing the torsion, and the surface of the connection between the beam and steel tube is bonded with a welded steel ring. They performed experiments on 14 CFST column-ring beam specimens subjected to a cyclic lateral load and studied the seismic performance of the ring beam joint. The joints exhibited good energy dissipation capacity, and the failure of the joint did not influence the load carrying capacity of the column. Han et al. [15] proposed two types of connections between a CFST column and RC beam: a ring steel plate, radial reinforcement, and steel brackets installed through the tubular core; and ring reinforcement welded to the tube and steel brackets installed through the tubular core. Shi et al. [16] suggested two types of connections for an outer-plated steel-concrete composite beam and CFST column. They carried out a low-cyclic reversed loading test and finite element simulation for the two types of joints and analyzed the performance in terms of the failure mode, hysteretic curve, strength, ductility, and strain of the steel bars, plates, and tubes. The results showed that both connections provided a high carrying capacity, ductility, and energy dissipation capacity. Nie et al. [17] and Bai et al. [18] proposed a new connection for concrete-encased CFST columns and RC beams. The steel tube is interrupted so that the RC beam is kept continuous in the joint zone, and multiple lateral hoops are used to guarantee the performance of the joint. They conducted experimental and theoretical studies on this approach. Zhang et al. [19] introduced another connection type: ring beam joints with a discontinuous outer tube between the concrete-filled twin steel tube columns and reinforced concrete beams. The seismic performance of the joints was evaluated through cyclic loading tests and numerical simulation. Their results showed that the joints satisfied seismic design principles. Chen at al. [20] investigated a type of through-beam connection between a CFST column and RC beam. The steel tube was entirely or partially cut at the location of the beam to keep the longitudinal steel rebar continuous. They performed experimental and finite element simulation analyses on this type of connection. Xu et al. [21] proposed a connection between a stiffened precast sleeve-connected CFST column and RC beam. They conducted low-cyclic reversed loading tests to consider the axial compression ratio and location of the connection. Their results showed that the connection had excellent load carrying capacity, energy dissipation capacity, and ductility. Chen et al. [22] and Yao et al. [23] considered engineering examples and researched CFST columns passing through rigid joints with circular, long, and rectangular openings. They showed that the main failure mode of the specimens was local buckling of the upper and lower reinforcement rings. The reinforcement of the joints after opening did not affect the bearing capacity of the columns and the short stiffener compensated for the weakening of the tube due to the opening. Zha et al. [24] carried out a low-cyclic reversed loading test and finite element simulation analysis on nonwelded CFST column-RC beam joints and showed that such joints demonstrated good ductility and energy dissipation capacity.

Although these joints have been applied to some engineering projects, each type has some disadvantages, such as difficulties in welding and pouring concrete into tubes because of corbels. In addition, the rebar in the joint area is arranged together more closely, which affects the quality of the poured concrete and the spatial use of the building.

In this study, small holes were opened in the steel wall of the CFST column, and longitudinal rebar was passed through the holes to form the RC beam. Two connection methods for the CFST column and RC beam are proposed: a vertical steel plate and studs and a U-shaped steel plate and studs. These connections can enhance the stiffness of the CFST column-RC beam joint. They are not only easy to apply to the structure but also provide other advantages, such as clear force transmission, good integrity, reduced material consumption, and convenient construction.

The proposed CFST column-RC beam joints have not previously been reported. In order to study the seismic performance of the CFST column and RC beam with steel plate-stud connections, three full-scale joint specimens were designed and fabricated. Low-cyclic reversed loading tests were performed to study the failure mode, failure mechanism, hysteretic curve, and skeleton curve. The results showed that the proposed joints have good mechanical properties and ductility, so they have a wide range of engineering applicability.

2. Types of Proposed Joints and Experimental Plan

2.1. New Joint Types and Details. This paper proposes steel plate-stud connection methods based on passing the longitudinal rebar of an RC beam through a CFST column. Specifically, small holes are made on the steel tube to pass the longitudinal reinforcement through so that the bending moment can be transferred. A segmental tube or steel plate is welded outside the section of the rebar holes to reinforce the CFST column and guarantee its performance. The vertical or U-shaped steel plate and studs are welded outside the steel tube to facilitate the transfer of the interfacial shear force between the RC beam and CFST column. Figure 1 shows the joint construction diagrams.

2.2. Experimental Program. In order to study the seismic behavior of the RC beam with the new connection types, three beam-column joints were designed in accordance with the current code's specifications of strong joints and weak members: XJJD, SSJD, and SUJD. XJJD was a common RC beam-column joint that was selected from the interior joints of a frame structure in a project. The specimen was taken from the middle part of a beam's reverse bending point. The column height was four times the diameter of the CFST column. The specimens were designed to be full scale. Figure 2 shows the sectional dimensions and reinforcement details of XJJD. SSJD and SUJD were CFST column-RC beam joints: SSJD was connected by studs and a vertical steel

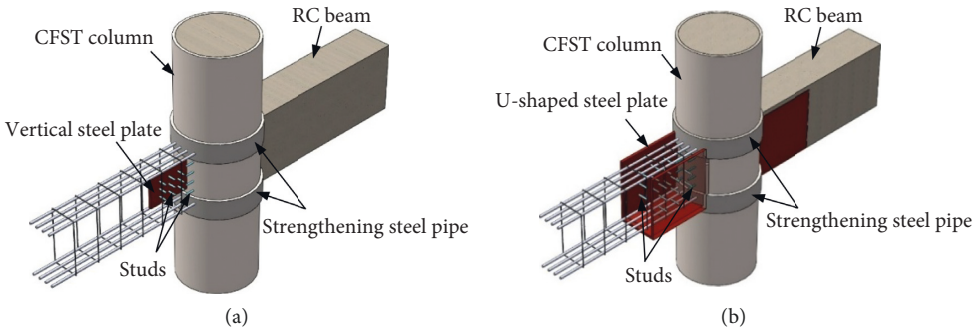

Figure 1: Schematic diagrams of the joints: (a) configuration of the steel plate-stud connection; (b) configuration of the U-shaped steel plate-stud connection.

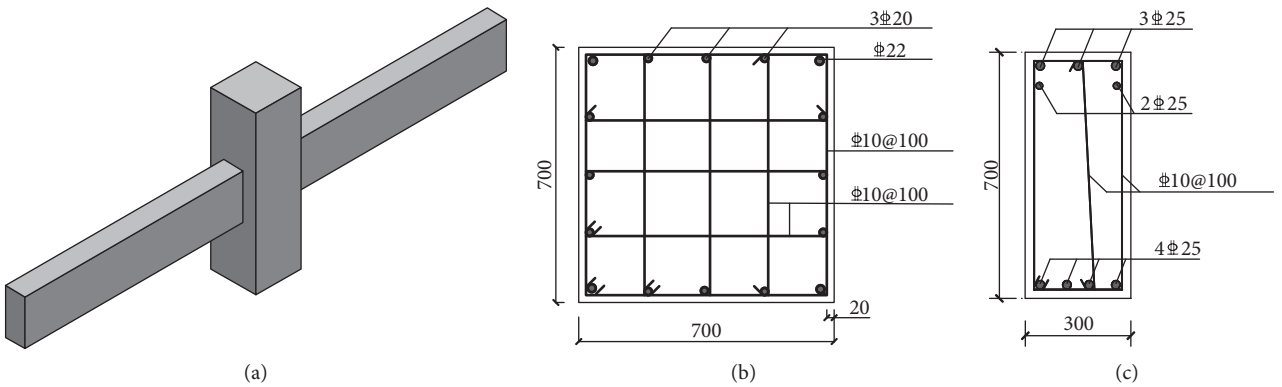

Figure 2: Sectional dimensions and reinforcement details of specimen XJJD: (a) schematic diagram, (b) column section, and (c) beam section.

plate, and SUJD was connected by studs and a U-shaped steel plate. Table 1 presents the main parameters of each specimen.

The sectional dimensions and reinforcement details for the beam were the same for all three specimens. The beam cross section was 300 mm × 700 mm. For reinforcement, 3Φ25 + 2Φ20 longitudinal rebars were distributed in two rows on the top of the beam section and 4Φ25 longitudinal rebars were distributed at the bottom. The stirrups were distributed to follow 3Φ10@100. All beams had a concrete strength grade of C35. The cross section of the RC column was 700 mm × 700 mm.

For the CFST specimens of SSJD and SUJD, the diameter of the CFST column was 610 mm, and the wall thickness was 10 mm. Small holes were made in the steel tube of the column with a diameter of 1.2d, where d is the diameter of the longitudinal rebar. The outside of the tube was reinforced by a steel plate welded on. Reinforced steel plates with the same holes ($b = 402$ mm, $h = 219$ mm, $t = 10$ mm; $b = 402$ mm, $h = 180$ mm, and $t = 10$ mm) were taken from a steel tube with a diameter of 630 mm and wall thickness was 10 mm. All of the steel tubes had a strength grade of Q345. The longitudinal rebar of the beam passed through the holes. Eight ML15 grade studs with a diameter of 16 mm and length of 100 mm were welded on the beam-column interface. The studs were distributed in four rows and two columns with both the horizontal and vertical spacing being 100 mm.

SSJD was the joint specimen connected by a vertical steel plate and studs. The vertical plate had a thickness of 6 mm, height of 350 mm, and length along the beam of 350 mm. Six ML15 grade studs with a diameter of 13 mm and length of 80 mm were welded on each side of the vertical steel plate. The studs were distributed in three rows and two columns with horizontal and vertical spacing of 110 and 90 mm, respectively. The details of the connection configuration are shown left in Figure 3(b).

SUJD was the joint specimen connected by a U-shaped steel plate and studs. The U-shaped steel plate had a thickness of 4 mm, height of 550 mm, and length along the beam of 350 mm. Six ML15 grade studs with a diameter of 13 mm and length of 80 mm were welded on each inner face for the two vertical plates of the U-shaped steel plate. The studs were distributed in three rows and two columns with horizontal and vertical spacing of 110 and 150 mm, respectively. The details of the connection configuration are shown right in Figure 3(b).

The joint specimens designed in this study follow the design concept of "strong column and weak beam, strong shear and weak bending, and strong joint and weak member" in the code for seismic design of building structures (GB50011-2010) [25]. According to the design code for concrete structures (GB50010-2010) [26], the design bending capacity of the RC beams M_b was 424.23 kN·m or −415.84 kN·m. The longitudinal rebars of beam section were

Table 1: Parameters of specimens.

Specimen no.	Column section size (mm)	Reinforcement in column	Column height H (mm)	Beam section size (mm)	Reinforcement in beam	Configuration of the beam-column connection
XJJD	700 × 700	Longitudinal bar 4ϕ22 + 12ϕ20 Stirrup: 5ϕ10@100	2440	300 × 700	Longitudinal bar top: 3ϕ25 + 2ϕ20	—
SSJD	610 × 10	—	2440	300 × 700	Bottom: 4ϕ25 stirrup: 3ϕ10@100	Vertical steel plate and studs
SUJD	610 × 10	—	2440	300 × 700		U-shaped steel plate and studs

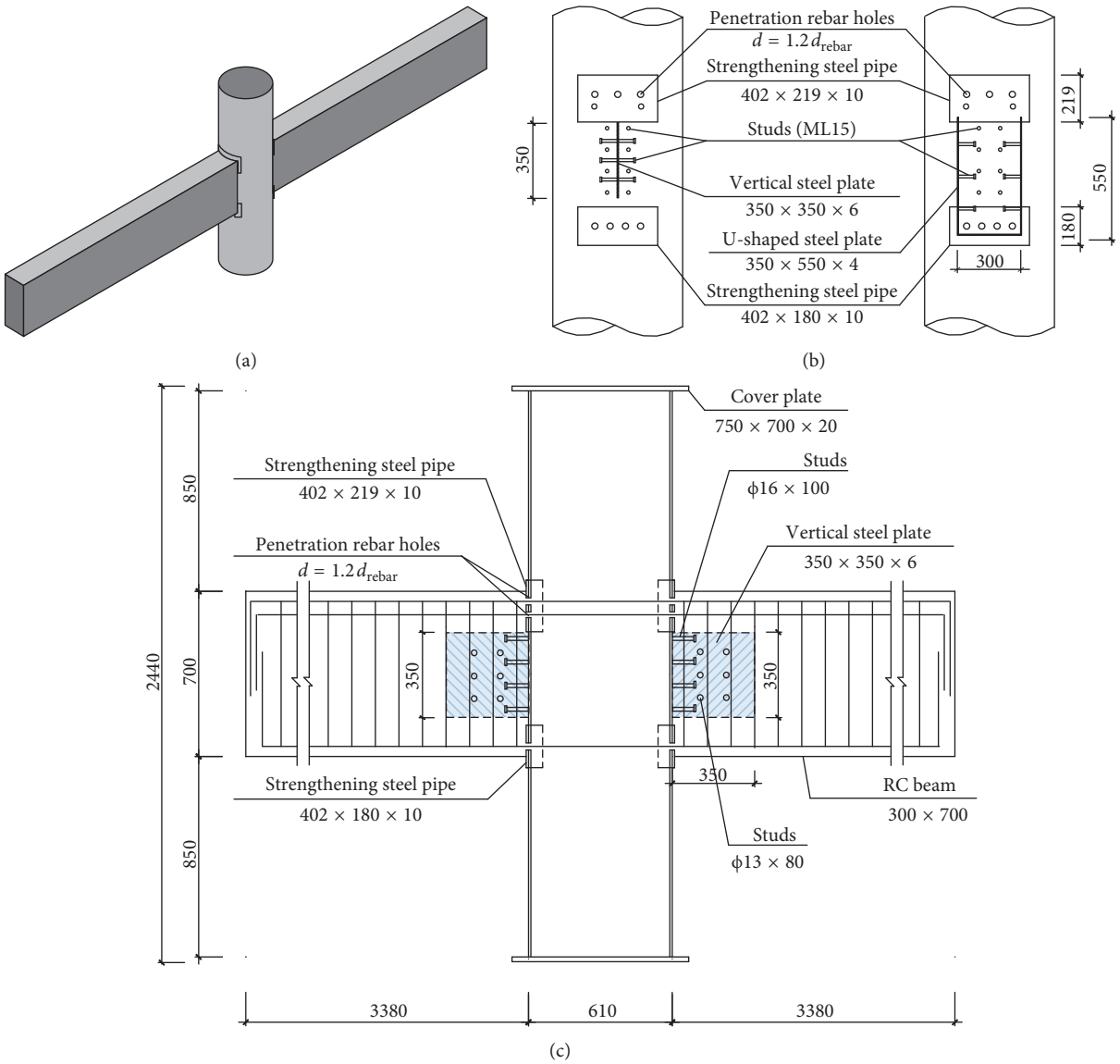

Figure 3: Continued.

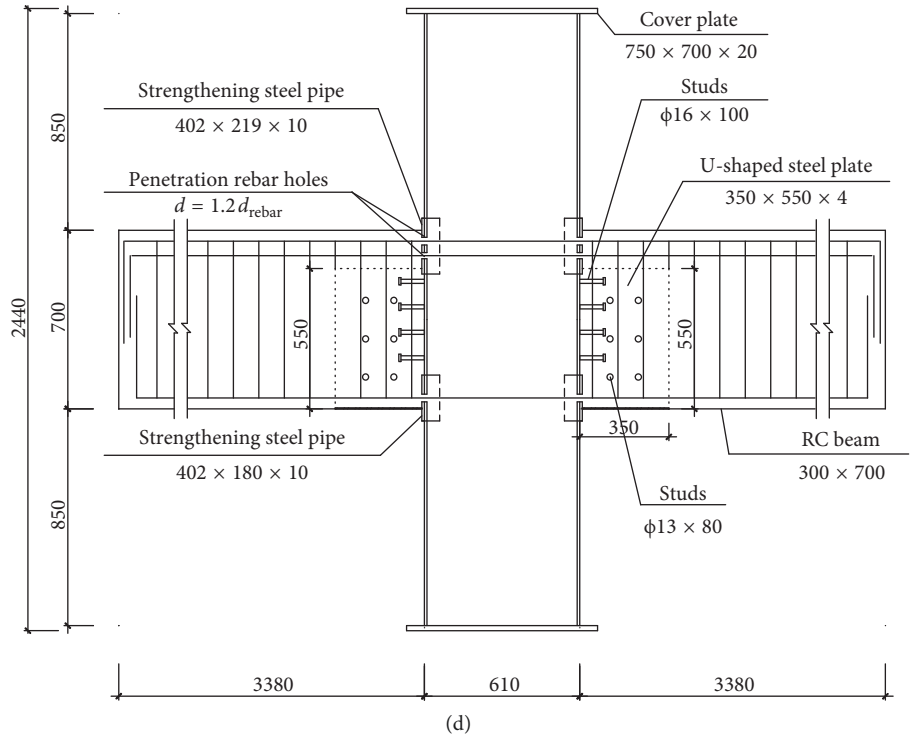

Figure 3: Sizes and connection configurations for specimens SSJD and SUJD: (a) schematic diagram of SSJD and SUJD; beam-column connections of (b) left: SSJD and right: SUJD; sectional views of (c) SSJD and (d) SUJD.

asymmetrical; for convenience, here the upper longitudinal reinforcement of the beam section was defined as positive when in tension, while the longitudinal reinforcement of the lower part was negative when in tension. The design shear capacity V_{cs} was 692.91 kN. For the RC columns, the design axial compressive capacity N_c was 11, 900.41 kN, the design bending capacity M_c was 1339.53 kN·m, and the design shear capacity V_c was 1826.47 kN. According to the technical code for CFST structures (GB50396-2014) [27], the design axial compressive capacity of the CFST columns N_{c0} was 16, 190.98 kN, the design bending bearing capacity M_{c0} was 1807.26 kN·m, and the design shear bearing capacity V_{c0} was 2429.28 kN. According to the code for seismic design of buildings (GB50011-2010), the design value of the combined shear force of the core area of the beam-column joints in XJJD V_j was 936.00 kN, and the shear capacity of the core section of the joint V_{jR} was 1741.3 kN. For SSJD and SUJD specimens, there is no formula for calculating the shear capacity of the core area of CFST column-RC beam joints in the current code, so the shear capacity of the core area of CFST column-RC beam joints was not checked in this study. The bearing capacities of the beam, columns, and joints were checked separately, and the results are presented in Table 2. The calculation results show that the three specimens all satisfy the design principles of "strong column and weak beam, strong shear and weak bending, and strong joint and weak member."

The SSJD and SUJD joint specimens in this study had a CFST column-RC beam structure connected by steel plates and studs. The connection structure of a steel plate and studs was used to ensure that the shear force on the beam could be transferred to the column through the steel plate and studs. The design value of the shear capacity was calculated separately for each specimen, and the results are listed in Table 3. The equations employed for connector design are as follows.

According to the design code for concrete structures (GB50010-2010), the design value of the shear capacity of the beam V_{cs} was calculated using

$$V_{cs} = \alpha_{cv} f_t b h_0 + f_{yv} \frac{A_{sv}}{s} h_0, \quad (1)$$

where α_{cv} is the shear capacity coefficient of the concrete in the inclined section, f_t is the design value of the axial tensile strength of concrete, b is the width of the beam section, h_0 is the effective height of the beam section, f_{yv} is the design value of the tensile strength of the stirrups, f_{yv} is the total cross-sectional area of each stirrup limb in the same cross section, and s is the spacing of stirrups along the length of the members.

According to the steel structure design standard (GB50017-2017) [28], the design value of the shear capacity of the interface connectors can be calculated using

$$V = V_s + V_p. \quad (2)$$

The design value of the shear capacity of the interface connectors consists of two parts: V_s, the total shear capacity of the welded studs on the wall of steel pipe, and V_p, the shear capacity of the vertical or U-shaped steel plate. These quantities can be calculated as follows:

Table 2: Specimen bearing capacities.

Check	Bending capacity ratio		Shear capacity ratio			Shear capacity of core area
Ratio	RC column/beam M_c/M_b	CFST column/beam M_{c0}/M_b	Beam V_{cs}/V'_{cs}	RC column V_c/V'_c	CFST column V_{c0}/V'_{c0}	XJJD V_{jR}/V_j
Result	3.16 (3.22)	2.56 (4.35)	4.30 (4.38)	1.19	1.17	1.86

Note. $V'_{cs} = M_b/L$, where L is the distance from the loading point to the end of the beam; $V'_c = M_c/H_c$, $V'_{c0} = M_{c0}/H_c$, H_c is the distance from the end of the column to the outside of the core area of the joint, and the values in parentheses are the results calculated with the longitudinal bar of the beam section under tension.

Table 3: Design values of the shear capacities of the beams.

Specimen no.	V_{cs} (kN)	V (kN)	V'_{cs} (kN)	V/V_{cs}	V_{cs}/V'_{cs}	Failure mode estimation
XJJD	692.91	—	161.30 (158.11)	—	4.30 (4.38)	Bending failure
SSJD	692.91	840.16	161.30 (158.11)	1.22	4.30 (4.38)	Bending failure
SUJD	692.91	940.70	161.30 (158.11)	1.36	4.30 (4.38)	Bending failure

Note. $V'_{cs} = M_b/L$, where L is the distance from the loading point to the end of the beam. The values in parentheses are the results calculated with the longitudinal bar of the beam section under tension.

$$V_s = 0.43 A_s \sqrt{E_c f_c} \le 0.7 A_s f_u \text{ (take the smaller value)},$$
$$V_p = V_{con} + V_{ps} \le f_v A_p \text{ (take the smaller value)}, \quad (3)$$

where f_u is the design value of the tensile strength of the studs, A_s is the sum of the cross-sectional areas of the studs, E_c is the elastic modulus of concrete, f_c is the design value of the compressive strength of concrete, V_{con} is the local bearing capacity of concrete, V_{ps} is the shear capacity of the studs on the vertical or U-shaped steel plate, f_v is the design value of the shear strength of the steel plate, and A_p is the cross-sectional area of the vertical or U-shaped steel plate.

The calculation results show that the shear capacities of the connectors are greater than those of the beams and that the shear forces generated by the bending resistance in the beams are less than the shear capacities of the beams, so the test specimens were predicted to undergo bending failure.

2.3. Material Properties. For all specimens, the reinforcement rebar had the Chinese grade HRB400. The steel tubes and plates were Q345 grade steel. ML15 grade studs were used in the proposed plate-stud connections. All beams were made of C35 grade concrete based on the Chinese design code (2010). All columns were made of C50 grade concrete. Tables 4 and 5 list the tested mechanical properties of the steel and concrete.

2.4. Test Setup and Loading Program. The tests were carried out with a 4000 kN multifunction electrohydraulic servo test system. Figure 4 shows the loading device. At the beginning of a test, a vertical load with an axial compression ratio of 0.3 was applied to the column and kept constant for the duration of the test. Then, antisymmetric loads were applied to both ends of the beam. Displacement control was adopted for the test. Before the specimen yielded, it was loaded in increments of 5 mm. After yielding was reached, the specimen was loaded in increments of the yield displacement. Two cycles were repeated for each level of displacement. The test was terminated when the specimen failed, which was defined as a decrease in the apparent load capacity to 85% of the maximum supported load. Figure 5 shows the loading program.

2.5. Measurement Contents and Method. For the test, the following were observed and measured: the vertical load at the top of the column, the vertical compressive and tensile forces at the beam end, the vertical displacement at the loading point of the beam end, the rotation and shear deformation of the plastic hinge area at the end of the beam, the crack development and failure mode of the specimen, etc. Figure 6 shows the instrumentation arrangement.

3. Test Results and Discussion

3.1. Failure Process and Failure Mode. The observed damage phenomena and failure mode were similar for each specimen. The failure process can be divided into three stages: cracking, yielding, and failure. Figure 7 shows the failure mode of each specimen. From the beginning of the test loading to the failure of the three specimens, the core area of the joints remained intact. No cracks were found in the core area of the XJJD specimen, and no obvious deformation was observed in the core area of the SSJD and SUJD specimens.

3.1.1. Failure Process of XJJD. The XJJD specimen was in the elastic state for the initial loading stage. After the first-level load (±5 mm) was applied, 3-4 microcracks occurred on the top and bottom of the south and north beams (Figure 6). When the second-level load was applied, the number of vertical microcracks on the sides of the beams increased, and some cracks occurred at the end of the beam. Existing cracks were also observed to extend. After the third-level load (±15 mm) was applied, the number of microcracks increased and the existing cracks continued to extend obliquely. The upper and lower two diagonal cracks developed to connect on each beam. The longitudinal reinforcement of the beam yielded at the fourth-level load (±20 mm). The existing

Table 4: Material properties of steel.

Material	Diameter (thickness) (mm)	Material grade	Yield strength f_y (MPa)	Ultimate strength f_u (MPa)	Elongation A (%)	Elastic modulus E_s (MPa)
Rebar	10	HPB400	413	607	22.06	1.8×10^5
	20	HRB400	430	559	20.13	2.0×10^5
	22	HRB400	436	617	19.50	2.0×10^5
	25	HRB400	436	608	19.93	2.0×10^5
Steel plate	4	Q345	395	530	19.03	2.1×10^5
	6	Q345	409	539	22.90	2.0×10^5
Steel tube	10	Q345	423	569	16.17	2.0×10^5
Stud	13	ML15	339	456	15.38	—
	16	ML15	340	457	15.40	—

Table 5: Material properties of concrete.

Strength grade	Axial compressive strength f_c (MPa)	Axial tensile strength f_t (MPa)	Elastic modulus E_c (MPa)
C35	29.2	2.48	3.34×10^4
C50	52.1	3.35	3.78×10^4

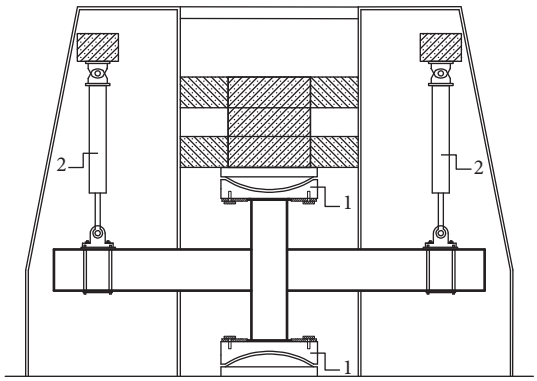

Figure 4: Test setup: (1) spherical hinge and (2) vertical actuator.

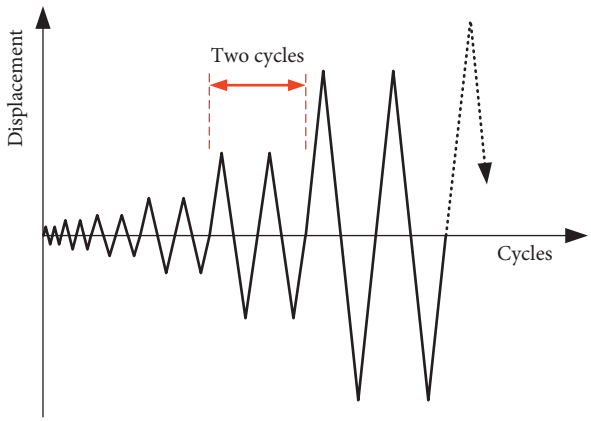

Figure 5: Loading history.

cracks were observed to widen and extend. The number of diagonal penetrating cracks increased to 5-6. The main diagonal penetrating cracks became wider upon further loading. When the sixth-level load (±3Δ) was applied, the cracks near the end widened, and the concrete was crushed with little spalling. The load on the south beam reached its maximum value. After the seventh-level load (±4Δ) was applied, the main diagonal cracks near the end of the beam widened further, and the concrete at the corner was crushed with spalling. When loaded to −4Δ, the north beam reached its peak load in the negative direction. When loaded to 5Δ, the concrete bulged within 30 cm from the end of the upper north beam. Meanwhile, the concrete bulged within 30 cm from the end of the lower south beam. The north beam reached the peak load in the positive direction. When loaded to −5Δ, the concrete on the upper part of the north beam end showed spalling and the longitudinal reinforcement buckled. The concrete had serious spalling within 20 cm from the end of the south beam. The longitudinal reinforcement and stirrups were visible in this area. After the ninth-level load was applied, the concrete spalled off within 40 cm from the end of the beam, the longitudinal reinforcement buckled, and the load resistance of the beam decreased. At this point, the specimen was destroyed. The crack development process is shown in Figure 8.

3.1.2. Failure Process of SSJD. The SSJD specimen was in the elastic state in the initial loading stage. After the first-level load (±5 mm) was applied, 4-5 microcracks were observed on the south and north beams. The number of microcracks on the sides of the beam increased after the second-level load was applied. The existing microcracks extended and three cracks within 1 m from the joint became connected. After the third-level load was applied, the number of cracks gradually increased. The existing vertical cracks extended to the end of the beam along the diagonal direction. Five cracks developed through both the south and north beams. The longitudinal reinforcement of the beam yielded at the fourth-level load (±20 mm). The number of connected cracks on both sides of the beam increased, but the crack width was still small. The cracks were distributed between the loading point and end of the beam. Compared with

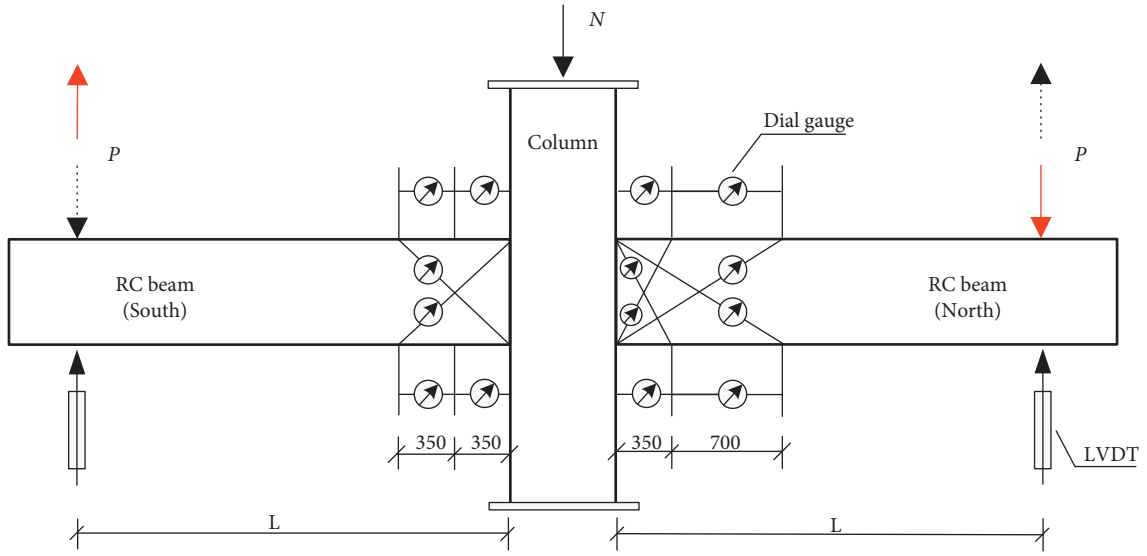

Figure 6: Installation positions of the dial gauges and linear variable differential transformers (LVDTs).

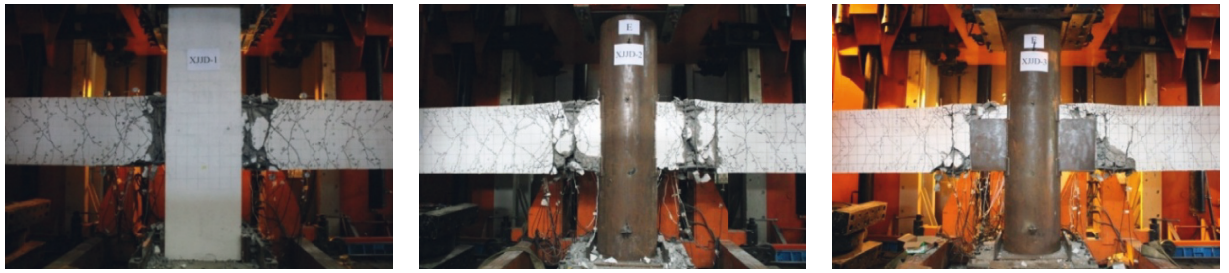

(a) (b) (c)

Figure 7: Failure modes of specimens: (a) XJJD, (b) SSJD, and (c) SUJD.

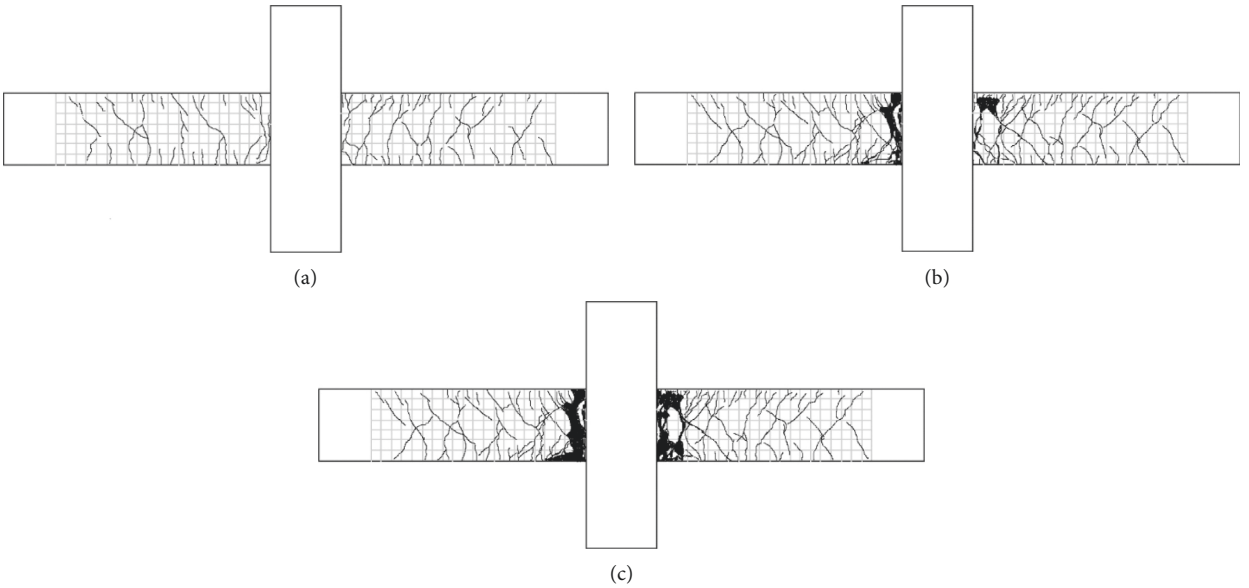

(a) (b) (c)

Figure 8: Crack development process of XJJD: (a) yielding stage, (b) peak load stage, and (c) failure mode.

XJJD, the cracks were more dispersed. After the fifth-level load (±2Δ) was applied, the number of cracks at the end of the beam increased and the existing cracks extended. The damage range of the beam end expanded. After the sixth-level load (±3Δ) was applied, cracks developed within 1 m from the ends of the north and south beams. Both the number and width of the cracks increased. When the seventh-level load was applied, the cracks at the end developed, and the main cracks 30–40 cm from the end widened. The concrete between the cracks showed slight spalling. After the eighth-level load (±5Δ) was applied, a large number of cracks occurred on the upper and lower parts of the beams, and the concrete was crushed. The cracks concentrated at 30–40 cm and 50 cm from the beam end showed clear widening. At this loading stage, both the south and north beams reached the peak loads in the positive and negative directions, respectively. When the seventh-level load (±6Δ) was applied, the concrete on the upper and lower sides of the south and north beams was crushed and spalled off. The rebar was exposed, and the longitudinal rebar of the two beam ends buckled. When loaded to −6Δ, the concrete within 30–60 cm from the end of the beam spalled off, and the load resistance of the beam decreased. At this point, the specimen was destroyed. Compared with XJJD, the main damage area of the beam end moved outward. Figure 9 shows the crack development process.

3.1.3. Failure Process of SUJD. The SUJD specimen was in the elastic state in the initial loading stage. After the first-level load (±5 mm) was applied, 4-5 microcracks occurred on the south and north beams. When the second-level load was applied, the number of cracks increased, and the existing cracks extended to form 3-4 connected cracks. After the third-level load was applied, some vertical cracks were observed in the area above the U-shaped steel plate. The number of new microcracks increased and was distributed over the RC beam. The existing cracks on the upper and lower parts of the beam developed along the diagonal direction, and the connected cracks increased to 5-6. When the fourth-level load (±20 mm) was applied, the longitudinal reinforcement of the beam yielded, the number of diagonal cracks increased, and the cracks widened. After the fifth-level load (±2Δ) was applied, both the number and width of the vertical and diagonal cracks increased. As the load was increased, the number of cracks on the upper part of the U-shaped steel plate and within 30 cm of the plate increased gradually. Some concrete spalling occurred at the outer edge of the U-shaped steel plate. The cracks near the U-shaped steel plate widened to form the main cracks. When the seventh-level load (±4Δ) was applied, the diagonal cracks within 40 cm of the U-shaped steel plate showed obvious widening. The vertical cracks on the upper side of the U-shaped steel plate also widened. The cracks were observed to extend and widen upon further loading. The concrete outside the bottom of the U-shaped steel plate was crushed and began spalling off. The concrete cracks along the upper part of the U-shaped steel plate widened and developed underneath the plate. The positive and negative peak loads were each reached at the eighth-level load. After the ninth-level load (±6Δ) was applied, the concrete outside the bottom of the U-shaped steel plate was severely crushed and fell off. The concrete at the upper part of the U-shaped steel plate was crushed and bulged. The rebar was exposed and buckled. The bearing capacity decreased, and at this point the specimen was destroyed. The crack development process is shown in Figure 10.

3.2. Load-Displacement Relationship. Figure 11 shows the load-displacement curves of each specimen. The first quadrant represents the upper reinforcement of the beam section in tension. A plumper hysteresis loops indicates a stronger energy dissipation capacity. The specimens were in the elastic stage and the hysteresis curves were almost linear in the initial stage of loading. The residual deformation was small after unloading in this stage. As the load increased, the stiffness of the load-displacement curves gradually decreased. The slopes of later loading curves were smaller than the second cycle at the previous load level. When the concrete spalled, the decrease in stiffness increased with the cycle times, and the degradation phenomenon became obvious. After the peak load, the strength degradation in the second cycle became noticeable. The three specimens had plump hysteretic curves. SUJD had the plumpest hysteretic curve and largest envelop area of the hysteretic loops.

3.3. Skeleton Curve. Figure 12 shows the skeleton curves for the specimens. Because of the asymmetric reinforcement of the beam section, the skeleton curves obtained with the low-cyclic reversed loading test differed. The elastic, yielding, and ultimate states of the three specimens were clearly observed. Table 6 lists the feature points of the test results. Table 7 presents the calculated average reaction forces of each specimen; the positive direction was as defined previously in the paper.

3.4. Analysis of the Bending Capacity of RC Beam with the Steel Plate-Stud Connection. According to the design code for concrete structures (GB50010-2010) [26], the bending capacity of RC beams is given by

$$\begin{aligned} \sum X &= 0, \\ \alpha_1 f_c b x &= f_y A_s, \\ \sum M &= 0, \\ M \le M_u &= \alpha_1 f_c b x \left(h_0 - \frac{x}{2}\right). \end{aligned} \tag{4}$$

The measured reaction forces at the loading point of the beam end were used to calculate the bending capacities M_b at the end of the beam and M_{bf} at the failure section. Based on the failure modes of the three specimens, the end of the beam was taken as the failure section of XJJD, and section 350 mm away from the end (i.e., the outer edge of the vertical

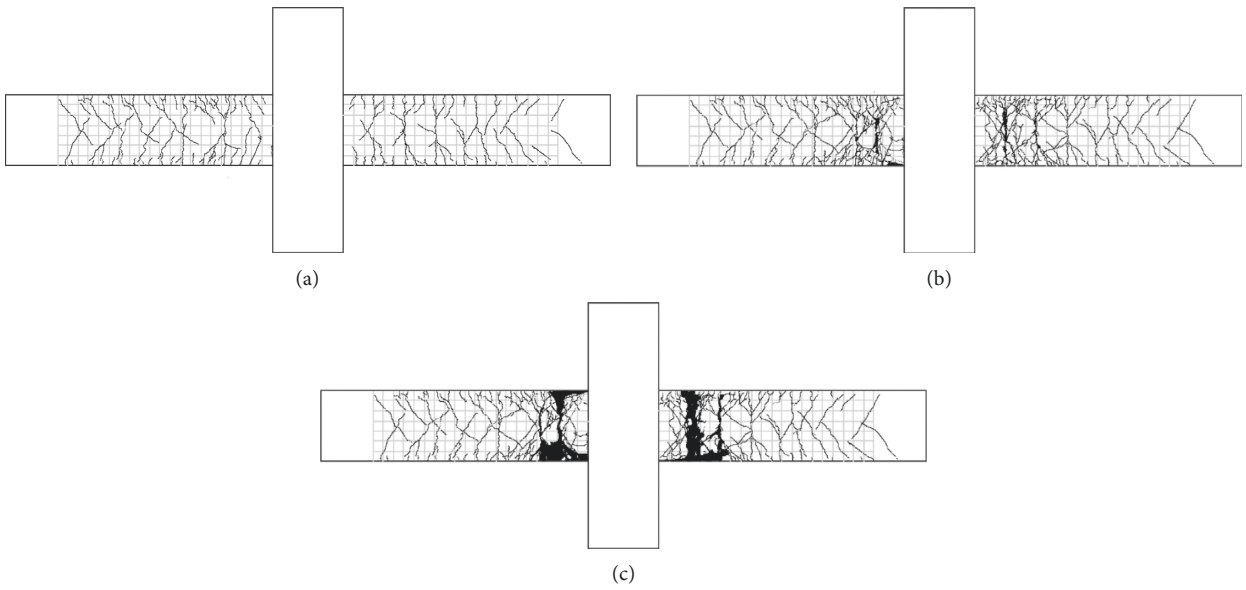

Figure 9: Crack development process of SSJD: (a) yielding stage, (b) peak load stage, and (c) failure mode.

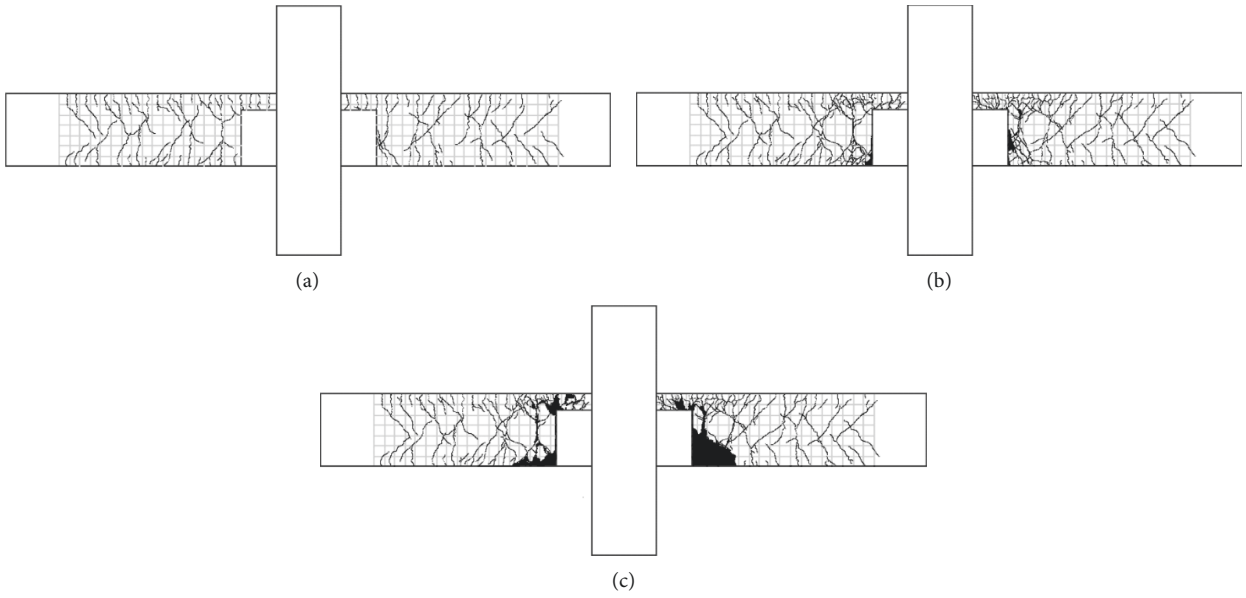

Figure 10: Crack development process of SUJD: (a) yielding stage, (b) peak load stage, and (c) failure mode.

or U-shaped steel plate) was taken as the failure section of SSJD and SUJD.

$$M_{\mathrm{b}} = \overline{F} \cdot L,$$
$$M_{\mathrm{bf}} = \overline{F} \cdot L_{\mathrm{f}}. \tag{5}$$

where $\overline{F}$ is the average reaction force at the ends of the south and north beams, L is the distance between the loading point and end of the beam (2590 mm for XJJD and 2635 mm for SSJD and SUJD), and L_{f} is the distance between the loading point and failure section.

The theoretical and experimental values of the bending capacity of the beams were calculated for loads in the positive and negative directions. Table 8 presents the results.

The results showed that the experimental bending capacity for each specimen was higher than the theoretical calculated values. Compared with the RC beam-column joint specimen XJJD, the bending capacity of SSJD and SUJD showed increases in the bending capacity at the end of the beam of 10.6% and 17.7%, respectively, under positive loading and 17.0% and 18.3%, respectively, under negative loading. For the failure section, the bending capacities of the three specimens were basically consistent: compared to XJJD, SSJD decreased by 4.1% and SUJD increased by 2.0% under positive loading and SSJD and SUJD at the end of the beam increased by 1.4% and 2.6%, respectively, under negative loading. In SSJD, the vertical steel plate and studs

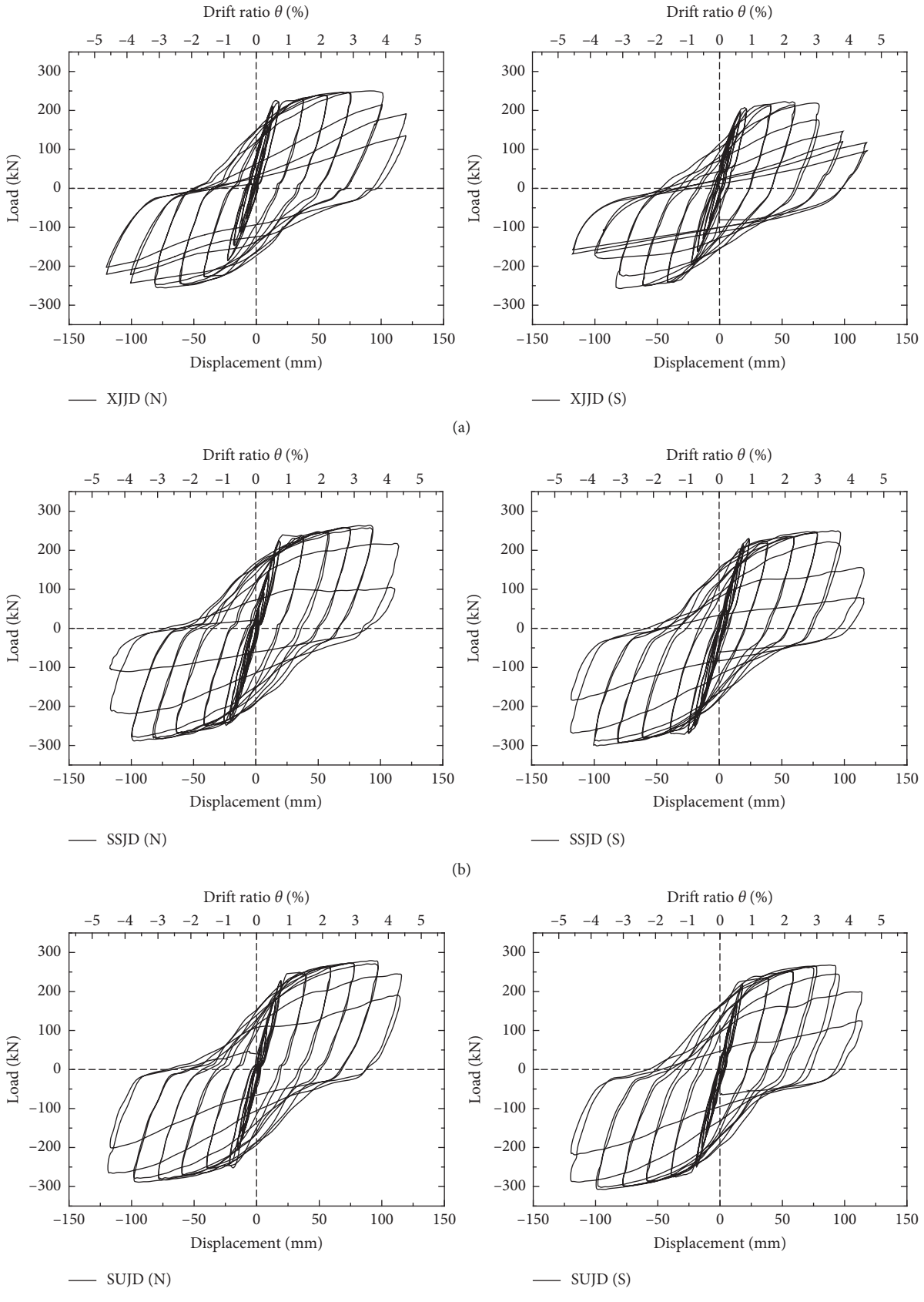

Figure 11: Load-displacement curves of specimens: (a) XJJD, (b) SSJD, and (c) SUJD.

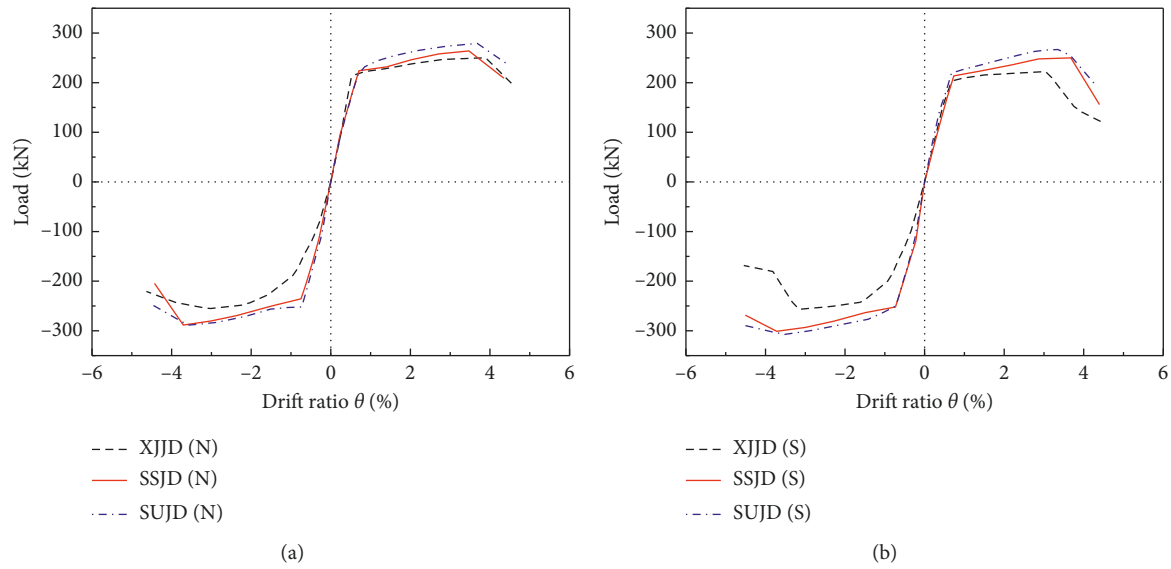

Figure 12: Skeleton curves for specimens: (a) north beam and (b) south beam.

Table 6: Test values of feature points of specimens.

Specimen no.	Position	Loading direction	Yield		Peak		Ultimate	
			Δ_y (mm)	P_y (kN)	Δ_{max} (mm)	P_{max} (kN)	Δ_u (mm)	P_u (kN)
XJJD	North beam	Positive	17.71	220.34	100.81	250.22	112.98	212.69
		Negative	−22.86	−184.33	−79.34	−255.55	−122.50	−217.22
	South beam	Positive	16.73	196.33	79.67	222.63	87.99	189.24
		Negative	−22.25	−195.34	−83.10	−257.17	−91.00	−218.59
SSJD	North beam	Positive	18.63	223.90	91.47	263.91	108.07	224.32
		Negative	−19.69	−235.62	−97.62	−288.47	−107.54	−245.20
	South beam	Positive	19.35	213.73	96.87	250.04	104.46	212.53
		Negative	−19.32	−251.96	−97.98	−301.00	−126.12	−255.85
SUJD	North beam	Positive	19.29	227.45	96.96	279.27	115.81	237.39
		Negative	−19.21	−251.93	−94.46	−288.77	−118.75	−245.45
	South beam	Positive	17.94	220.51	92.93	267.66	104.23	227.51
		Negative	−18.90	−249.64	−93.30	−307.61	−121.53	−261.47

Table 7: Average peak loads.

Specimen no. loading direction		North beam F (kN)	South beam F (kN)	Average $\overline{F}$ (kN)
XJJD	(+)	250.22	222.63	236.43
	(−)	255.55	257.17	256.36
SSJD	(+)	263.91	250.04	256.98
	(−)	288.47	301.00	294.74
SUJD	(+)	279.27	267.66	273.47
	(−)	288.77	307.61	298.19

Table 8: Bending bearing capacity of each specimen.

Specimen no. loading direction		M_u (kN·m)	M_b (kN·m)	M_{bf} (kN·m)
XJJD	(+)	533.37	612.34	612.34
	(−)	522.61	663.97	663.97
SSJD	(+)	533.37	677.13	587.19
	(−)	522.61	776.63	673.47
SUJD	(+)	533.37	720.58	624.87
	(−)	522.61	785.73	681.36

were set at the end of the beam, which improved the local stiffness and made the failure area move away from the end of the beam. In SUJD, the U-shaped steel plate and studs were set at the end of the beam and the concrete in this area was constrained by the U-shaped steel plate. Thus, the cracks were restrained during the loading process.

3.5. Displacement Component. The total displacement Δ of the beam end mainly comprises the bending deformation Δ_f, shear deformation Δ_s, and slip deformation Δ_{slip}. Figure 13 shows a diagram of each deformation. The values measured by the dial gauges shown in Figure 6 and the following equations were used to calculate the displacements of each stage.

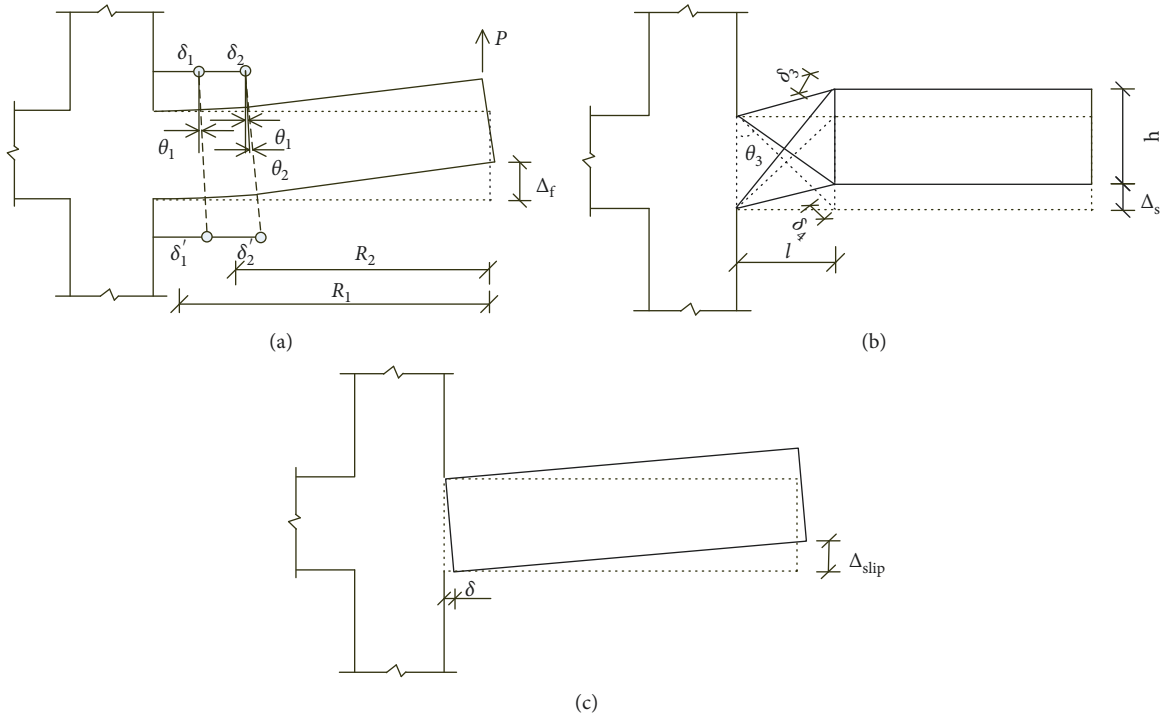

Figure 13: Three main deformation components: (a) bending, (b) shear, and (c) sliding.

The total bending deformation Δ_f caused by the rotation of the beam hinge in the plastic hinge region is given by

$$\Delta_f = \delta_{b1} + \delta_{b2}. \tag{6}$$

The deflection of the beam end δ_{b1} caused by the rotation of the plastic hinge region can be calculated from the measured average rotation of the section:

$$\begin{aligned} \delta_{b1} &= \theta_1 R_1 + \theta_2 R_2, \\ \theta_1 &= \frac{(\delta_1 + \delta_1')}{h_1}, \\ \theta_2 &= \frac{(\delta_2 + \delta_2')}{h_2}, \end{aligned} \tag{7}$$

where θ_1, θ_2 are the average rotations of the section of the plastic hinge region; $\delta_1, \delta_2, \delta_1', \delta_2'$ are the elongation and compression measured by the dial gauges on the upper and lower surfaces of the beam; and h_1, h_2 are the distances between the upper and lower dial gauges on the beam.

Beyond the plastic region, the bending deformation δ_{b2} of the beam is calculated according to elastic theory:

$$\delta_{b2} = \frac{P(L-l)^3}{3E_c I_e}, \tag{8}$$

where P is the load applied at the beam end, $(L-l)$ is the length of the beam from outside the plastic hinge region to the loading point, E_c is the elastic modulus of concrete, and I_e is the effective moment of inertia of the beam ($I_e = 0.5I_g$; I_g is the gross section moment inertia).

The shear deformation of the plastic hinge region is shown in Figure 13(b). The shear deformation Δ_s at each stage is calculated as follows:

$$\begin{aligned} \Delta_s &= \frac{|\delta_3| + |\delta_4|}{2\cos\theta_3}, \\ \cos\theta_3 &= \frac{h}{\sqrt{l^2 + h^2}}, \end{aligned} \tag{9}$$

where δ_3, δ_4 are the elongation and compression of the dial gauges along the diagonal direction of the plastic hinge region; h is the height of the beam section; l is the length of the plastic hinge region; and the slip deformation Δ_{slip} is given by $\Delta_{slip} = \Delta - \Delta_f - \Delta_s$.

The displacement Δ' is caused by bending, shear, and slip within l of the plastic hinge region:

$$\Delta' = \delta_{b1} + \Delta_s + \Delta_{slip}. \tag{10}$$

Table 9 lists the calculation results for the components of the total displacement at the beam end. The bending deformation Δ_f accounted for 78%–95% of the total displacement Δ. The plastic hinge region total displacement Δ' accounted for over 79% of the total displacement Δ. The total displacement Δ of the beam end mainly comprised the bending deformation Δ_f, shear deformation Δ_s, and slip deformation Δ_{slip}. Bending accounted for the largest proportion of deformation among the components.

3.6. Stiffness Degradation. The stiffness degradation reflects the effect of accumulated damage on the structure and refers to the increase in the peak displacement with the cycle times

Table 9: Test results of the deformation.

Specimen no.	Feature state	δ_{b1} (mm)	Δ_s (mm)	Δ_{slip} (mm)	Δ' (mm)	δ_{b2} (mm)	(δ_{b1}/Δ) (%)	(Δ_f/Δ) (%)	(Δ'/Δ) (%)
XJJD	Yield	13.27	0.62	0.36	14.25	3.46	74.9	94.5	80.5
	Peak	79.74	9.69	7.45	96.88	3.93	79.1	83.0	96.1
	Ultimate	90.84	12.42	6.38	109.64	3.34	80.4	83.4	97.0
SSJD	Yield	12.90	0.50	1.45	14.85	3.78	69.2	89.5	79.7
	Peak	75.78	6.69	4.55	87.02	4.45	82.8	87.7	95.1
	Ultimate	90.03	9.54	5.31	104.88	3.19	83.3	86.3	97.0
SUJD	Yield	13.03	0.48	1.94	15.45	3.84	67.5	87.4	80.1
	Peak	75.86	9.65	6.74	92.25	4.71	78.2	83.1	95.1
	Ultimate	87.19	15.24	9.38	111.81	4.00	75.3	78.7	96.5

when the peak cycle load is maintained. In this study, the secant stiffness was used to evaluate the stiffness degradation. Figure 14 shows the stiffness attenuation curve. There were some differences between the positive and negative initial stiffness, which was mainly because of the asymmetric reinforcement of the beam section. Under cycle loading, the specimen accumulated damage, and the stiffness in the positive and negative directions gradually approached each other. The initial stiffness in the negative direction was greater for SUJD and SSJD than for XJJD. The configurations of the U-shaped and vertical steel plates and studs increased the negative initial stiffness of the specimen. The three specimens showed similar failure processes. When the concrete was not cracked, the specimens were basically in the elastic stage, and the stiffness was very high. As the load and displacement increased, the stiffness gradually decreased. When the concrete spalled off, the reduction in stiffness increased with the number of load cycles, which indicated obvious degradation.

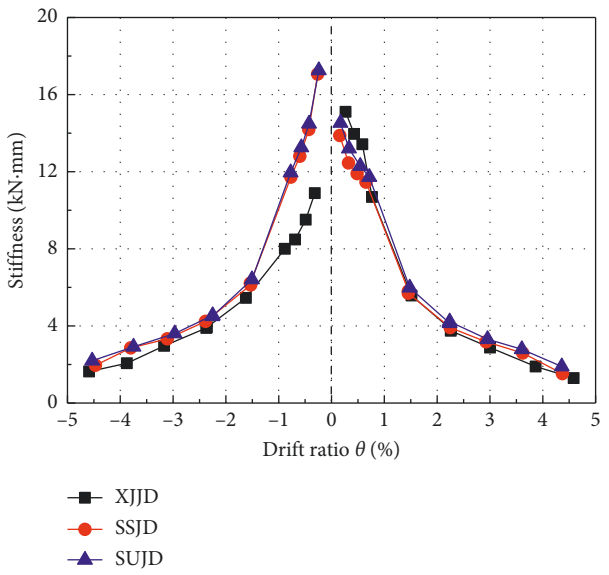

Figure 14: Stiffness attenuation curves of the specimens.

3.7. Displacement Ductility. In this study, the displacement ductility coefficient was used to reflect the ductility performance of the specimen and is defined as the ratio of the ultimate displacement to the yield displacement. The displacement ductility coefficients of the three specimens were all higher than 4.0, and all specimens had good deformation capacity. Compared with XJJD, SSJD and SUJD showed increases in the displacement ductility coefficient of 10.1% and 15.6%, respectively. Table 10 lists the displacement ductility results.

Table 10: Ductility coefficients of the specimens.

Specimen no.	Position	Ductility coefficient (+)	Ductility coefficient (−)	Average value
XJJD	North beam	6.38	5.36	5.27
	South beam	5.26	4.09	
SSJD	North beam	5.80	5.46	5.80
	South beam	5.40	6.53	
SUJD	North beam	6.00	6.18	6.11
	South beam	5.81	6.43	

3.8. Energy Dissipation Capacity. The energy dissipation capacity of components is an important index for evaluating the seismic performance. The area surrounded by a hysteretic loop is the energy dissipated by a component for one cycle loading. A larger value indicates a better seismic performance by the specimen. In this study, the average energy dissipation coefficient μ_e and equivalent viscous damping ratio ξ_e were used to evaluate the energy dissipation capacity of the joints:

$$\mu_e = \frac{E_{sum}}{mE_y}, \tag{11}$$

where E_{sum} is the sum of the energy dissipation of each cycle and is obtained from the area of the hysteresis curve, m is the number of cycles after yielding, and $E_y = P_y \cdot \Delta_y/2$ is the nominal elastic energy.

$$\xi_e = \frac{1}{2\pi} \cdot \frac{S_{(ABC+CDA)}}{S_{(OBE+ODF)}}, \tag{12}$$

where $S_{(ABC+CDA)}$ is the area enclosed by the hysteretic curve in Figure 15, and $S_{(OBE+ODF)}$ is the sum of the areas of ΔOBE and ΔODF in Figure 15.

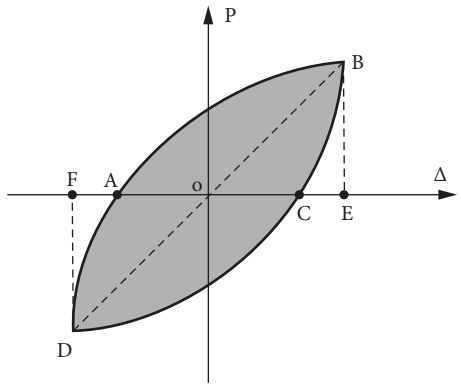

Figure 15: Schematic diagram for the calculation of the equivalent viscous damping coefficient.

The average areas surrounded by the hysteretic curves of the north and south beams were calculated as the total energy dissipation. Figure 16 shows the total energy consumption of each specimen. Table 11 lists the calculated average energy dissipation coefficients. Compared with XJJD, SSJD and SUJD showed increases in the cumulative energy dissipation of 23.0% and 25.8%, respectively. SUJD showed energy consumption about 2.2% higher than that of SSJD. SSJD and SUJD had higher average energy dissipation coefficients than XJJD, which indicates that the proposed joints have a significantly higher energy dissipation capacity than ordinary RC joints. Table 12 lists the equivalent viscous damping ratios $\xi_{e,y}$, $\xi_{e,p}$, and $\xi_{e,4.5\%}$ of the yield point, peak load point, and maximum deformation point ($\theta = 4.5\%$), respectively. At the yielding point, XJJD had a slightly greater equivalent viscous damping ratio than SSJD and SUJD. However, after the peak load was reached, SSJD and SUJD had greater equivalent viscous damping ratios than XJJD. The specimens with plate-stud connections showed good energy dissipation capacity.

Figure 17 shows the relationship between the equivalent damping ratio and drift ratio for the three specimens. From the initial loading stage to yielding, the envelope area of the hysteretic loop was small, and the equivalent viscous damping coefficient decreased. The energy dissipation capacity of each specimen increased with the displacement until the drift ratio reaches 3%. When the drift ratio exceeded 3%, the energy dissipation of XJJD decreased, while the equivalent viscous damping ratios of SSJD and SUJD still grew slowly and became larger than that of XJJD at the ultimate displacement.

4. Conclusions

(1) Two kinds of plate-stud connections pierced with longitudinal rebars are proposed for CFST column-RC beam joints. The bending moment at the end of the beam is transmitted by the longitudinal rebar of the beam, which is consistent with the traditional RC structure. The shear force at the end of the beam is transmitted by the plate and studs, which is similar to the CFST column-steel beam structure. The mechanism of force transmission is clear.

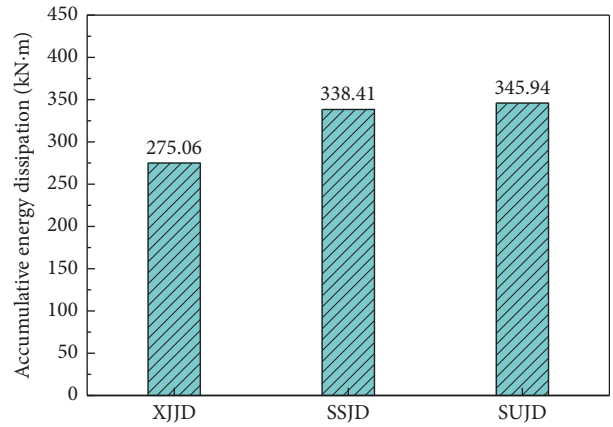

Figure 16: Accumulative energy dissipation of each specimen.

Table 11: Average energy dissipation coefficient.

Specimen no.	E_{sum} (kN·m)	μ_e
XJJD	275.06	13.89
SSJD	338.41	15.20
SUJD	345.94	15.47

Table 12: Equivalent damping ratio.

Specimen no.	$\xi_{e,y}$	$\xi_{e,p}$	$\xi_{e,4.5\%}$
XJJD	0.137	0.288	0.244
SSJD	0.110	0.312	0.304
SUJD	0.089	0.303	0.280

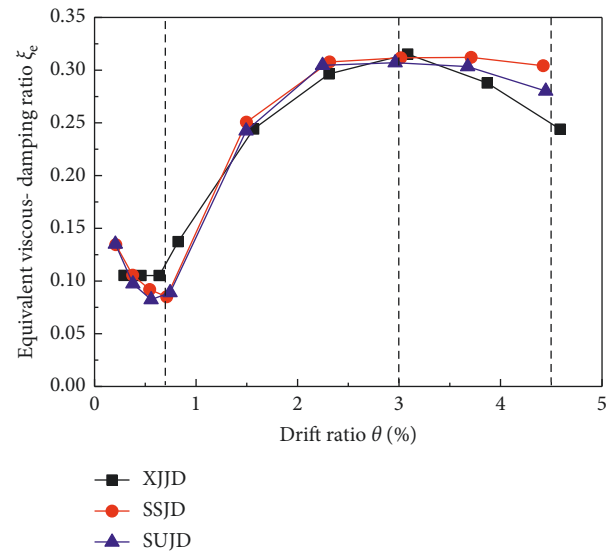

Figure 17: Equivalent damping ratio.

(2) For CFST column-RC beam joints connected by a plate and studs with a shear span ratio of 4, the deformation of the longitudinal rebar at the end of the beam is consistent with that of the RC joint under a low-cyclic load. There is no shear slip at the beam-

column interface. The load-displacement hysteretic curve is plump, and the joint has a good connection performance.

(3) The failure mode of CFST column-RC beam joints with plate-stud connections is similar to that of traditional RC joints, but the damage region mainly occurs outside the connecting steel plate, and the plastic hinge shifts outward.

(4) For the CFST column-RC beam joint with steel plate-stud connections, the calculated bending capacity at the failure section of the beam was basically consistent with that of RC joints. The bending capacity of the vertical and U-shaped plate-stud connection joints at the end of the beam showed increases of about 10.6% and 17.7%, respectively, in the positive direction and 17.0% and 18.3%, respectively, in the negative direction.

(5) Compared with the RC joint, the energy dissipation of the CFST column-RC beam joints with vertical and U-shaped plate-stud connections increased about 23.0% and 25.8%, respectively. The average energy dissipation coefficient increased by 9.4% and 11.4%, respectively. The equivalent damping ratio increased by 10.1% and 15.6%, respectively.

Data Availability

The program and experimental data used to support the findings of this study are available from the corresponding author upon request.

Conflicts of Interest

The authors declare that there are no conflicts of interest regarding the publication of this paper.

Acknowledgments

This research was funded by the National Key Basic Research and Development Program of China (grant no. 2016YFC0701100) and Dalian Wanda Commercial Real Estate Co., Ltd.

References

[1] M. Tomii, K. Sakino, K. Watanabe, and Y. Xiao, "Lateral load capacity of reinforced concrete short columns confined by steel tube," in *Proceeding of the International Speciality Conference on Concrete Filled Steel Tubular Structures*, Harbin Institute of Technology, Harbin, China, August 1985.

[2] J. Liu, S. Zhang, X. Zhang, and L. Guo, "Behavior and strength of circular tube confined reinforced-concrete (CTRC) columns," *Journal of Constructional Steel Research*, vol. 65, no. 7, pp. 1447–1458, 2009.

[3] S. Morino, M. Uchikoshi, and I. Yamaguchi, "Concrete-filled steel tube column system-its advantages," *International Journal of Steel Structures*, vol. 1, no. 1, pp. 33–44, 2001.

[4] A. Elremaily and A. Azizinamini, "Experimental behavior of steel beam to CFT column connections," *Journal of Constructional Steel Research*, vol. 57, no. 10, pp. 1099–1119, 2001.

[5] J. Beutel, D. Thambiratnam, and N. Perera, "Cyclic behaviour of concrete filled steel tubular column to steel beam connections," *Engineering Structures*, vol. 24, no. 1, pp. 29–38, 2002.

[6] K.-J. Shin, Y.-J. Kim, Y.-S. Oh, and T.-S. Moon, "Behavior of welded CFT column to H-beam connections with external stiffeners," *Engineering Structures*, vol. 26, no. 13, pp. 1877–1887, 2004.

[7] L.-Y. Wu, L.-L. Chung, S.-F. Tsai, C.-F. Lu, and G.-L. Huang, "Seismic behavior of bidirectional bolted connections for CFT columns and H-beams," *Engineering Structures*, vol. 29, no. 3, pp. 395–407, 2007.

[8] D. Zhang, J. Zhao, and Y. Zhang, "Experimental and numerical investigation of concrete-filled double-skin steel tubular column for steel beam joints," *Advances in Materials Science and Engineering*, vol. 2018, Article ID 6514025, 13 pages, 2018.

[9] D. A. Nethercot, T. Q. Li, and B. Ahmed, "Unified classification system for beam-to-column connections," *Journal of Constructional Steel Research*, vol. 45, no. 1, pp. 39–65, 1998.

[10] R. Bjorhovde, A. Colson, and J. Brozzetti, "Classification system for beam-to-column connections," *Journal of Structural Engineering*, vol. 116, no. 11, pp. 3059–3076, 1990.

[11] L. M. Xiang and X. L. Lv, "Introduction to joints of CFST high rise building," *Structural Engineers*, vol. 2000, no. 4, pp. 1–5, 2000, in Chinese.

[12] J. Cai and T. Y. Huang, "The application status and existing problems of CFST joint," *Building Structure*, vol. 31, no. 7, pp. 8–10, 2001, in Chinese.

[13] H. L. Lu, J. M. Wu, and C. X. Xu, "Selection and design of joints for CFST frame," *Journal of Wuhan University of Technology*, vol. 26, no. 2, pp. 44–46, 2004, in Chinese.

[14] X. D. Fang, S. Y. LI, J. R. Qian, and R. Q. Yang, "Experimental research on seismic behavior of concrete filled steel tubular column-ring beam joint under cyclic loading," *Journal of Building Structures*, vol. 23, no. 6, pp. 10–18, 2002, in Chinese.

[15] X. L. Han, R. B. He, and J. Ji, "Experimental research on CFST connections with ring plate and steel corbels through the core," *Industrial Construction*, vol. 35, no. 11, pp. 21–24, 2005, in Chinese.

[16] Q. Y. Shi, F. Ding, Y. Xuan, and A. Q. Li, "Experimental investigation on joints connecting outer-plated steel-concrete composite beam and concrete filled steel tube column," *Engineering Mechanics*, vol. 28, no. 4, pp. 109–115, 2011, in Chinese.

[17] J. Nie, Y. Bai, and C. S. Cai, "New connection system for confined concrete columns and beams. I: experimental study," *Journal of Structural Engineering*, vol. 134, no. 12, pp. 1787–1799, 2008.

[18] Y. Bai, J. Nie, and C. S. Cai, "New connection system for confined concrete columns and beams. II: theoretical modeling," *Journal of Structural Engineering*, vol. 134, no. 12, pp. 1800–1809, 2008.

[19] Y. F. Zhang, J. H. Zhao, and C. S. Cai, "Seismic behavior of ring beam joints between concrete-filled twin steel tubes columns and reinforced concrete beams," *Engineering Structures*, vol. 39, pp. 1–10, 2012.

[20] Q.-J. Chen, J. Cai, M. A. Bradford, X. Liu, and Z.-L. Zuo, "Seismic behaviour of a through-beam connection between concrete-filled steel tubular columns and reinforced concrete beams," *Engineering Structures*, vol. 80, pp. 24–39, 2014.

[21] S. Y. Xu, Z. L. Li, H. J. Liu, J. Jiang, and A. L. Jiao, "Seismic behavior of precast sleeve-connected CFST column to RC beam connection," *Journal of Harbin Institute of Technology*, vol. 48, no. 6, pp. 124–131, 2016, in Chinese.

[22] H. T. Chen, S. H. S. H. Wu, Y. F. Xiao, J. L. Zhang, and M. X. Lv, "The experimental research of steel bar passed through rigid joint of CFST frame," *Journal of Harbin University of Civil Engineering and Architecture*, vol. 32, no. 2, pp. 21–25, 1999, in Chinese.

[23] G. H. Yao, Y. Y. Chen, Y. J. Huang, D. H. Pan, X. Y. Zheng, and W. J. XU, "Experimental study on seismic behavior of joint of CFST column-RC beam," *Industrial Construction*, vol. 41, no. 2, pp. 97–101, 2011, in Chinese.

[24] X. Zha, C. Wan, H. Yu, and J.-B. M. Dassekpo, "Seismic behavior study on RC-beam to CFST-column non-welding joints in field construction," *Journal of Constructional Steel Research*, vol. 116, pp. 204–217, 2016.

[25] China Ministry of Construction, *Code for Seismic Design of Buildings (GB50011-2010)*, China Architecture & Building Press, Beijing, China, 2010, in Chinese.

[26] China Ministry of Construction, *Code for Design of Concrete Structures (GB50010-2010)*, China Architecture & Building Press, Beijing, China, 2011, in Chinese.

[27] China Ministry of Construction, *Technical Code for Concrete Filled Steel Tubular Structures (GB 50936-2014)*, China Architecture & Building Press, Beijing, China, 2014, in Chinese.

[28] China Ministry of Construction, *Code for Design of Steel Structure (GB50017-2017)*, China Architecture & Building Press, Beijing, China, 2017, in Chinese.